frontiers | Frontiers in Physics

TYPE Original Research
PUBLISHED 21 February 2023
DOI 10.3389/fphy.2023.1127505

OPEN ACCESS

EDITED BY
Tonglei Cheng,
Northeastern University, China

REVIEWED BY
Yue Wu,
Beijing Information Science and Technology University, China
Muguang Wang,
Beijing Jiaotong University, China
Zhongwei Tan,
Beijing Jiaotong University, China

*CORRESPONDENCE
Xiao Liang,
xiaoliang@muc.edu.cn

SPECIALTY SECTION
This article was submitted to Optics and Photonics, a section of the journal Frontiers in Physics

RECEIVED 19 December 2022
ACCEPTED 30 January 2023
PUBLISHED 21 February 2023

CITATION
Liang X and Zuo B (2023), A precision refractometer using strict dual-mode elliptical multilayer-core fibers with temperature and strain decoupled. *Front. Phys.* 11:1127505. doi: 10.3389/fphy.2023.1127505

A precision refractometer using strict dual-mode elliptical multilayer-core fibers with temperature and strain decoupled

Xiao Liang[1]* and Binzhou Zuo[2]

[1]School of Information Engineering, Minzu University of China, Beijing, China, [2]College of Science, Minzu University of China, Beijing, China

To accurately measure the surrounding refractive index (SRI), an all-fiber microstructure multi-parameters optical sensor based on Mach–Zehnder interferometer (MZI) has been designed. A homemade elliptical multilayer-core fiber (EMCF), in which only two modes could be propagated, is used in this sensor. This sensor has a sandwich structure of EMCF-SMF-EMCF (ESE). The sensitivities of RI, temperature, and strain are analyzed practically, and different from each other which would provide a basis for restraining cross-sensitivity of sensor and improving measuring precision. According to the numerical simulation, the relationship between the guided mode and relevant excitation coefficient is shown, and the sensing characteristic of the interference spectrum is well expatiated. Maximum sensitivities of ~31.83 nm per refractive index unit (RIU), ~69 pm/°C, and ~2.06 pm/με have been experimentally achieved. The monitoring system is promoted by the fact that the resonance dips have their individual sensitivities, and the standard matrix inversion method is used for simultaneous three parameters determination. Consequently, this fiber sensor could ensure the completion of accurate SRI measurements with temperature and strain decoupled.

KEYWORDS

strict dual-mode fiber, fiber sensor, mulit-parameters, axial micro-strain, in-fiber MZI

1 Introduction

The reliable and compact fiber sensors are significantly indispensable in many fields due to their unique characteristics, such as extremely high sensitivity and precision, stable electric insulation, chemical stability, resistance to electromagnetic interference, distributed measurement, and durability. Therefore, the fiber sensor has drawn a great deal of attention in various fields, such as the securities and protection monitoring [1, 2], biomedical instruments [3, 4], the construction industry [4, 5], aerospace [6, 7], etc. Apart from the above, the fiber sensor has the potential research values in measuring the surrounding refractive index (SRI). Compared with the conventional refractometer, which is mostly based on electrical and mechanical technologies [8], the fiber-optic SRI sensor has the advantages of compact size, anti-electromagnetic interference, high voltage, and corrosion resistance. However, due to the higher order modes guided in fibers, a stable clean interference spectrum would be hardly obtained. In addition, due to the temperature and axial micro-strain cross-sensitivity, the fiber-based refractometer could hardly achieve high-accuracy survey as well.

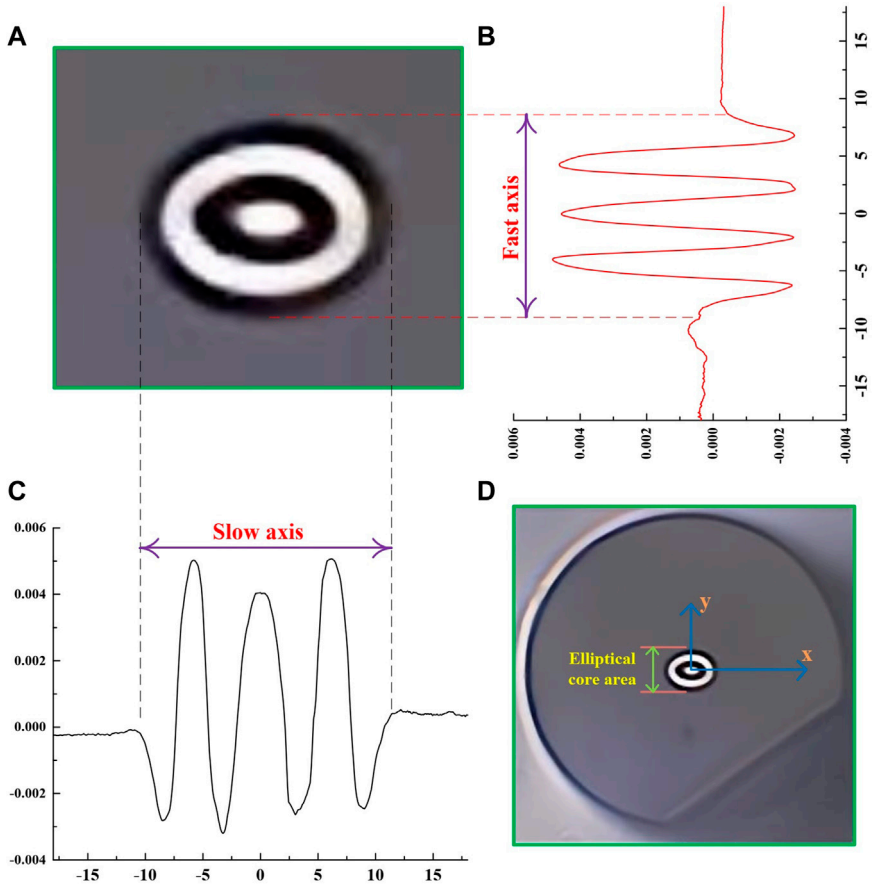

FIGURE 1
Schematic diagrams of **(A)** the cross-section micrograph of the elliptical core area; **(B)**, **(C)** the index profile along the fast/slow axis; and **(D)** the cross-section microstructure of the EMCF.

To attain a stable clean interference spectrum, the number of guided modes in the fiber must be limited, and the energy occupation of each mode should be roughly the same [9]. To restrict the number of interference modes, some solutions like using few modes fiber (FMF) have been demonstrated, such as temperature and strain sensors using an elliptical central silica core [10], gas concentration measurement based on the dual-mode Fiber Bragg Grating (FBG) structure [11], dual-parameter active fiber sensor based on a fiber ring laser [12], liquid-core optical fiber [13], and et al. A novel SRI sensor based on a specially designed polyimide coated dual-mode fiber (DMF) is presented by Lei [14]. The structure of this fiber is fabricated with an inner core, three inner claddings, and a pure silica outer cladding, which only permits the fundamental mode, LP_{01}, and the higher order core mode, LP_{02}, to propagate. However, higher order modes could be propagated in the round-core fiber, which leads to an unstable interference spectrum. In addition, the perturbance of temperature and micro-strain in the refractometer could also cause an unpredictable disturbance. Several schemes have been proposed to remove one interfering component, such as the temperature-compensated refractometer [15], and the refractometer with strain-error correction [16]. Moreover, there are some schemes proposed for the simultaneous measurement of them. A novel fiber-optic refractometer is proposed with its temperature and axial strain compensation [17]. This literature demonstrates a scheme using a tapered bend-insensitive fiber. However, numerous nanoscale gas-filled voids are embedded in its cladding, making it complex and a little repeatable. This study aims to develop a precision refractometer using homemade elliptical multilayer-core fibers (EMCF) with EMCF-SMF-EMCF (ESE) structure. Based on the in-fiber Mach–Zehnder interferometer (MZI), this refractometer is proposed and experimentally characterized.

This sensor has the advantage of a stable structure and is relatively easy to be fabricated. Furthermore, it could simultaneously measure SRI, temperature, and axial micro-strain. The transmission dips have their individual sensitivities. Thus, the temperature could be compensated, and axial micro-strain error could be corrected, which leads to an improvement in SRI measurement. In addition, by utilization of the EMCF, the higher order modes are suppressed, and it could only support the LP_{01} and LP_{11}^{even}, while the LP_{11}^{odd} would be suppressed by the elliptical fast-axis [18]. This strict dual-mode EMCF would enable this sensor to

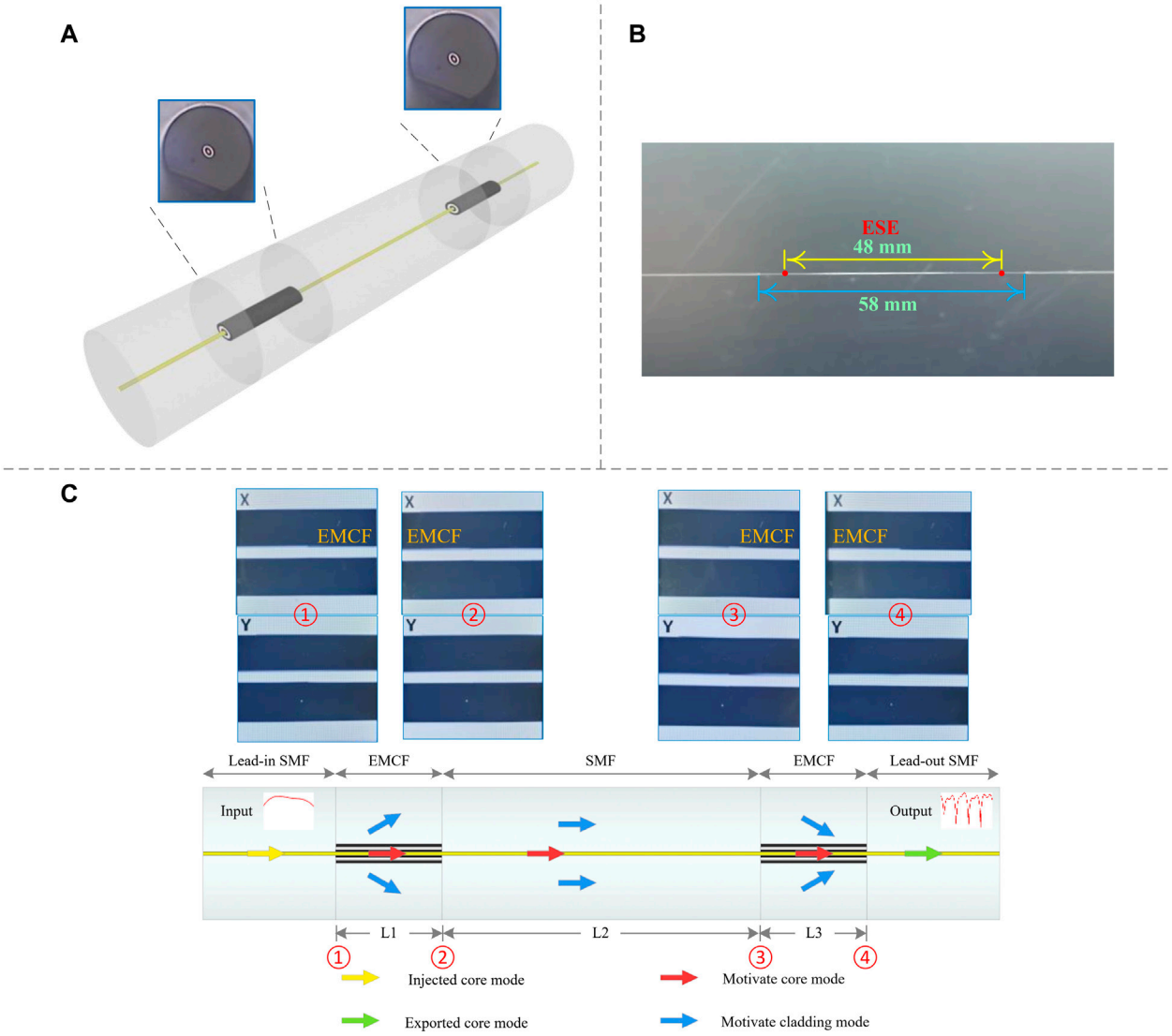

FIGURE 2
Details of the proposed sensor, **(A)** the three-dimensional structure; **(B)** the close view and geometrical sizes; **(C)** the representation and operation.

achieve a stable and clean interference spectrum [19]. Consequently, the multi-parameter monitor is easy to carry out by the wavelength shift. A detailed analysis of the mode interference is proposed. The operation mechanism and methods for characteristic compensation are demonstrated in elaborate experiments.

2 Design and principles of operation

2.1 Structure of the EMCF

This homemade strict dual-mode EMCF could be obtained with conventional modified chemical vapor deposition (MCVD) and solution-doping techniques. It is composed of an elliptical core area and conventional cladding. Figure 1A illustrates the cross-section micrograph of the elliptical core area, while the cross-section microstructure of the EMCF is shown in Figure 1D. It could be found from Figures 1A, D that the elliptical core area consists of a central elliptical core and three inner elliptical layers. The elliptical core area has a slow/fast axis with a length of 22.64/18.05 μm, and the diameter of the fiber is 125 μm. This special structure guarantees the feasibility of the strict dual-mode operation, which will be described in more detail later.

Figures 1B, C depict the distribution of the refractive index (RI), which is gained by an optical fiber analyzer (EXFO NR9200). This alternating low and high refractive index in the elliptical ring structure is acquired by doping with fluorine and germanium. The EMCF has a conventional cladding, the gray part, whose RI is 1.444. The highest RI of the slow/fast axis could achieve about 1.449/1.4485, while the lowest part could be approximately 1.4408/1.4415. The RI distribution is non-

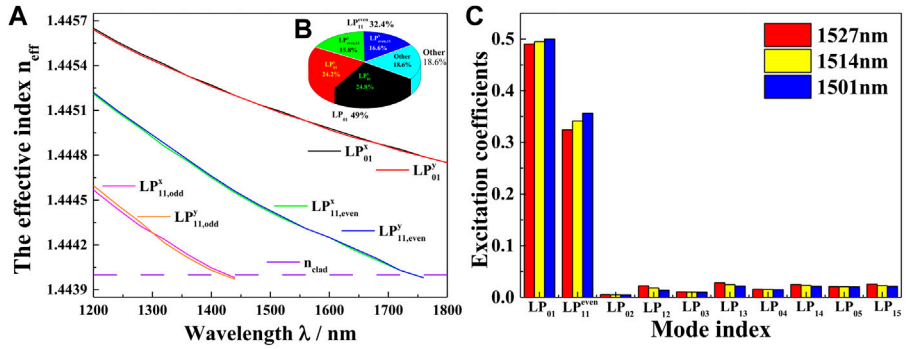

FIGURE 3
The guided-mode propagation analysis in EMCF, **(A)** the curves of λ vs. n_{eff} of the guided modes; **(B)** excitation coefficients for different modes in 1,510 nm; **(C)** excitation coefficients of various modes for various wavelength propagating in the first EMCF.

uniform and not strictly axisymmetric, which might have some influence on the mode distribution [20].

2.2 Configuration of the sensor and transmission principle

A fiber sensor, an in-fiber MZI based on ESE, has been utilized, and schematically plotted in Figure 2A and widely detailed in Figure 2C. It has a symmetrical ESE structure in that two same EMCFs are spliced to each end of a central SMF (Corning SMF-28). Then, two segments of SMF are stitched to the opposite ends of the ESE, playing the role of input and output SMF, respectively. Each segment is combined by the fiber fusion splicer (Fujikura, FSM-100M/P). As depicted in Figure 2B, the ESE is 48 mm long, which is 10 mm less than the total length of the sensor. This compact size enables this sensor to have a great potential for development and application in the field of micro-sensing. In more detail, the EMCF and central SMF lengths are 5 mm and 38 mm, respectively. This geometrical size is specially designed for an ideal coupling ratio of the propagating modes, which would be discussed in detail later.

Figure 2C shows the basic sensing principle of the sensor. A Gaussian beam is injected into the lead-in SMF, playing the role of the light source. Before reaching the central SMF, whose core and cladding act as the two arms of MZI, the fundamental modes (LP_{01}) and other cladding modes are excited by the first EMCF. As all the cladding modes have been coupled back to the core area by the second EMCF, an interference spectrum could be obtained in the lead-out SMF [21]. The SRI, temperature, and axial micro-strain could influence the optical path difference (OPD) of the LP_{01} and other modes. Hence, this device has the potential to measure the three parameters simultaneously. In addition, the fused splice losses between each EMCF and SMF, which correspond to Point 1 to Point 4, are 0.16 dB, 0.26 dB, 0.25 dB, and 0.16 dB, respectively. To have a high extinction radio MZI, the major axes of two EMCFs should be aligned, and the rotation angle of this two fibers should be specially arranged. The manufacturing approach is referenced to [22]

As mentioned above, the largest RI difference in the core area is only 0.0082, which satisfies the weakly guiding approximation [23].

By accumulating all the excited modes, which could be described as normalized and orthogonal wave functions, the total optical field distribution $\psi(x, y, z)$ is derived as

$$\boldsymbol{\psi}(\boldsymbol{x},\boldsymbol{y},\boldsymbol{z}) = \sum_{\boldsymbol{n}}^{\boldsymbol{N}} \boldsymbol{\eta_n}\boldsymbol{\psi_n^E}(\boldsymbol{x},\boldsymbol{y})\boldsymbol{e}^{-\boldsymbol{i}\boldsymbol{\beta_n}\boldsymbol{z}} \tag{1}$$

Where N is the number of excited modes in the EMCF. η_n, $\psi_n^E(x, y)$, β_n are excitation coefficient, guided mode distribution, and the longitudinal propagation constant in the EMCF, respectively. n represents a particular mode. Theoretically, the total field distribution is nearly the same as the incident field distribution. At the $z = 0$ position, the excitation coefficient, η_n, could have the expression in the form as [24]

$$\boldsymbol{\eta_n} = \frac{\iint \boldsymbol{\psi_n^S}(\boldsymbol{x},\boldsymbol{y})\boldsymbol{\psi_n^E}(\boldsymbol{x},\boldsymbol{y})\boldsymbol{dxdy}}{\iint \boldsymbol{\psi_n^E}(\boldsymbol{x},\boldsymbol{y})\boldsymbol{\psi_n^E}(\boldsymbol{x},\boldsymbol{y})\boldsymbol{dxdy}} \tag{2}$$

Where $\psi_n^S(x, y)$ is the incident field distribution in the input SMF.

Figure 3A describes the curves of different effective refractive index n_{eff} vs. wavelength λ. According to the optical waveguide theory [27], the cutoff wavelengths of LP_{11}^{even} and LP_{11}^{odd} are not the same, which is different from that of the conventional circular optical fiber. This happens because the effective index is related to the geometric size of the elliptical axis. Consequently, the LP_{11}^{even} has a higher cut-off wavelength than that of LP_{11}^{odd}. With a wavelength ranging from 1,425 nm to 1,575 nm, only the LP_{01} and LP_{11}^{even} could be propagated in the elliptical waveguide system. As a result, the EMCF could be considered as a distinct dual-mode fiber, which could only support four orthogonal polarization modes.

According to the definition of the half beat length L_π [24]

$$\boldsymbol{L_\pi} = \frac{\boldsymbol{\pi}}{\boldsymbol{\beta_{LP_{01}}} - \boldsymbol{\beta_{LP_{11}^{even}}}} \tag{3}$$

Where the propagation constants of LP_{01} and LP_{11}^{even} are represented as $\beta_{LP_{01}}$ and $\beta_{LP_{11}^{even}}$, respectively. In this sensor, the EMCF is 5 mm long, which is approximate eleven times of $\frac{L_\pi}{2}$. Hence, according to the coupled mode theory [23], the coupling ratio could achieve approximately 3 dB. As shown in Figure 3B, in the first EMCF, the

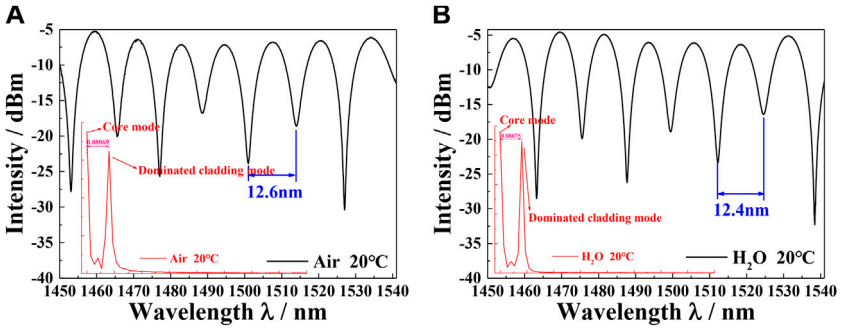

FIGURE 4
Interference-pattern analysis: the measured transmission spectrum and corresponding spatial frequency of the EMCF-based MZI in **(A)** air/ **(B)** water.

excitation coefficient of LP_{01} is 49%, and the one of LP_{11}^{even} is 32.4%. Other modes, which occupied 18.6%, are depicted in Figure 3C. Most obviously, the two mode groups, LP_{01} and LP_{11}^{even}, are dominant. In contrast, other higher order modes are so weak that they could be neglected. The reason why the higher order modes could be excited is that the coating of the EMCFs is removed completely. However, most of them would reduce exponentially because of weakly bound [9].

According to the definition of the normalized constant V_n [9]

$$V_n = \frac{2\pi}{\lambda} R\sqrt{n_{co}^2 - n_{cl}^2} \tag{4}$$

Where λ is the operation wavelength, R is the diameter geometry of the fiber, n_{co}/n_{cl} is the index of core/cladding. Since the normalized constant V_n of the EMCF varies in the different working wavelengths, the excitation coefficients among the three wavelengths are slightly different. In this case, a stable and clean interference spectrum could be gained.

Figure 4 shows the transmission spectrum and the free spectral range (FSR). As depicted, the interference spectrum is clean and stable. Since the two dominant mode groups have a close excitation coefficient, this phenomenon could be explained by the distinct dual-mode interference process. Therefore, regardless of other modes, the FSR could be described as [25].

$$FSR \approx \frac{\lambda^2}{\Delta n_{LP}^S L_S + 2\Delta n_{LP}^E L_E} \tag{5}$$

Where $\Delta n_{LP}^S/\Delta n_{LP}^E$ is the refractive index difference between modes LP_{01} and LP_{11}^{even} in the central SMF/EMCF. L_S and L_E are the lengths of the central SMF and EMCF, respectively. The FSRs in the air and water are the distance of the adjacent resonance dips, which are 12.6 nm and 12.4 nm, respectively. The spatial frequency is gained by the Fast Fourier Transform (FFT). The distance between the two peaks is 0.08069/nm in air and 0.08075/nm in water. The two peaks show that there are mainly two modes with similar power. However, there are some evanescent modes, which would cause some effect on the sensitivity and drift direction of the interference dips. To sum up, a clean and stable interference spectrum could be obtained by taking advantage of the strict dual-mode EMCF and controlling its length. The distinct FSR between each resonance dip is conducive to multi-parameter sensing because it could support a cleaner dip-drift spectrum. In addition, more accurate parameter sensitivities could be achieved. Finally, the conventional demodulation algorithm could be more simple and more precise.

2.3 Sensing principle

According to the optical waveguides theory [20], compared with LP_{01}, the LP_{11}^{even} has a lower effective refractive index, who has a low optical waveguide confinement property. Furthermore, the ESE structure has no coating, decreasing the absorption of radiation modes. As a result, LP_{11}^{even} modes could be propagated in the cladding of the central SMF. The sensing principle is based on the multimode interference (MMI) effect. The OPD between these two modes could be influenced by the environment which could change the effective refractive index and the L_S. Regardless of the much shorter part, L_E , the phase delay $\Delta\phi^{ij}$ could be expressed as [17]

$$\Delta\phi^{ij} \approx \frac{2\pi\left(n_{eff}^{01} - n_{eff}^{ij}\right)L_S}{\lambda} = \frac{2\pi\Delta n_{eff}^{ij} L_S}{\lambda} \tag{6}$$

Where n_{eff}^{01} and n_{eff}^{ij} are the effective refractive index of LP_{01} and a higher order mode, respectively. Δn_{eff}^{ij} is the effective refractive index difference between these two modes. The extinction radio of the interference spectrum could reach optimal performance, as $\Delta\phi^{ij} = 2n\pi$. Regardless of the evanescent modes, we could replace Eq. 6 by

$$\lambda_n \approx \frac{\Delta n_{eff}^{ij} L_S}{n} \tag{7}$$

Where λ_n is the wavelength of the nth resonance dip. As a result, $\lambda_n \approx \frac{\Delta n_{eff}^{ij} L_S}{n}$. In practical application, λ_n could be influenced by axial micro-strain, temperature, and SRI simultaneously.

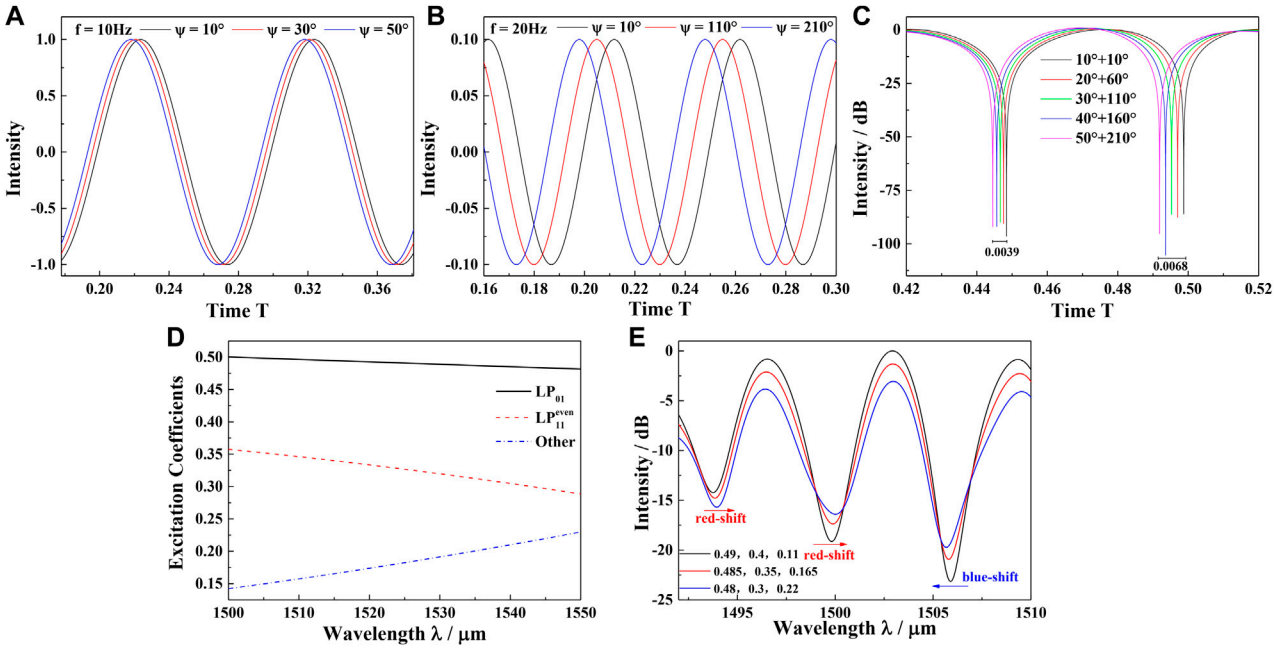

FIGURE 5
The mechanism analysis of the spectra shift, **(A)**, **(B)**, **(C)** the different sensitivities of the dips as the variation of the ψ; **(D)**, **(E)** the different shift directions as the variation of the excitation coefficients.

When axial micro-strain serves as the only source of interference, the change of λ_n caused by axial micro-strain could be described by [25]

$$\Delta\boldsymbol{\lambda}_{n,S} = -(\mathbf{1} + \mathbf{2}\boldsymbol{\mu} + \boldsymbol{p}_e)\boldsymbol{\lambda}_n\Delta\boldsymbol{\varepsilon} = \boldsymbol{C}_S^n\Delta\boldsymbol{\varepsilon} \tag{8}$$

Where $\Delta\lambda_{n,S}$ is the variation of λ_n caused by micro strain, μ is the Poisson ratio, and p_e is the effective strain-optic coefficient. For most silica fibers, μ and p_e value 0.16 and 0.22, respectively. $\Delta\varepsilon = \frac{\Delta L_{SMF}}{L_{SMF}}$, is the variation of axial micro-strain. Thus, C_S^n is a coefficient only related to material type. Therefore, the axial micro-strain could be determined by the shift of resonance wavelength.

Overlooking the affect by axial micro-strain and SRI, the change of λ_n caused by temperature, $\Delta\lambda_{n,T}$, could be obtained as [26]

$$\Delta\boldsymbol{\lambda}_{n,T} = (\boldsymbol{\delta} + \boldsymbol{\zeta})\boldsymbol{\lambda}_n\Delta\boldsymbol{T} = \boldsymbol{C}_T^n\Delta\boldsymbol{T} \tag{9}$$

Where δ and ζ are the thermal optical coefficient and dilatation coefficient respectively. For certain materials, δ and ζ are two constants. ΔT is the fluctuating temperature. C_T^n is a constant only changed by the material type. Thus, by monitoring the wavelength drift, we could obtain the exact variation of the surrounding temperature.

When only SRI is considered, n_{eff}^{01} would remain stable because of its deep location. Hence, the wavelength of the nth resonance dip influenced by SRI, $\lambda_{n,R}$, could be expressed as follows

$$\boldsymbol{\lambda}_{n,R} \approx \frac{\left(\boldsymbol{n}_{eff}^{01} - \boldsymbol{n}_{eff,R}^{ij}\right)\boldsymbol{L}_S}{\boldsymbol{n}} \tag{10}$$

Where $n_{eff,R}^{ij}$ is the effective refractive index of a higher order mode influenced by SRI. Then the variation of λ_n caused by SRI, $\Delta\lambda_{n,R}$, satisfies a similar equation [26]

$$\Delta\boldsymbol{\lambda}_{n,R} \approx \frac{-\Delta\boldsymbol{n}_{eff,R}^{ij}}{\Delta\boldsymbol{n}_{eff}^{ij}}\boldsymbol{\lambda}_n \approx \frac{-\boldsymbol{K}}{\Delta\boldsymbol{n}_{eff}^{ij}}\boldsymbol{\lambda}_n\Delta\boldsymbol{n}_R = \boldsymbol{C}_R^n\Delta\boldsymbol{n}_R \tag{11}$$

Where Δn_R is the SRI variation, K is the proportionality between Δn_R and $n_{eff,R}^{ij}$. $\frac{\lambda_n}{\Delta n_{eff}^{ij}}$ is a fixed constant as mentioned above. Generally, the relationship between Δn_R and $n_{eff,R}^{ij}$ tend to be non-linear. However, in this experiment, the range of Δn_R is strictly limited. Hence, $n_{eff,R}^{ij}$ could have a nearly linear increase with the increase of SRI. As a result, C_R^n is a fixed value as C_T^n and C_S^n. Similarly, by measuring the variation of λ_n, the SRI could be gained.

In addition, the sensitivity of each dip is different due to higher modes, which would be demonstrated with emulation and experiment results. To sum up, C_R^n, C_T^n, and C_S^n provide an opportunity to construct a character matrix for precision SRI sensing. Thus, this sensor could facilitate discrimination among the SRI, the temperature, and micro-axial strain, achieving accurate SRI measurement with temperature and axial strain compensations.

The essential condition to facilitate discrimination among these three parameters is differences in drift-sensitivity and drift-direction for environment variables. This phenomenon is caused by the higher order modes and has been analyzed in Figure 5. Based on the waveguide property, different Δn_{eff}^n would cause different interference frequencies, f. Various f could cause various phase delays, Ψ, as the variation of the environment. To better explain this phenomenon, the frequency components are taken analogous to sinusoids in the time domain. The interference pattern produced by LP_{01} and LP_{11}^{even} is depicted in Figure 5A. Qualitatively, it processes a wide range of intensity and a lower f, compared with the other interference pattern, Figure 5B, which is caused by LP_{01} modes and higher order modes. Regardless of the various intensity and other contributing factors, the MMI effect is taken analogous to sinusoids

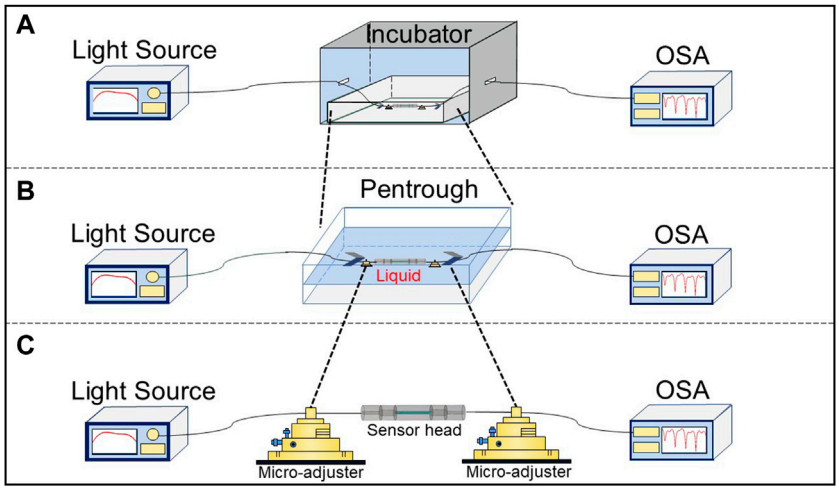

FIGURE 6
The schematic diagram of experimental setup for **(A)** temperature, **(B)** SRI, and **(C)** strain measurement.

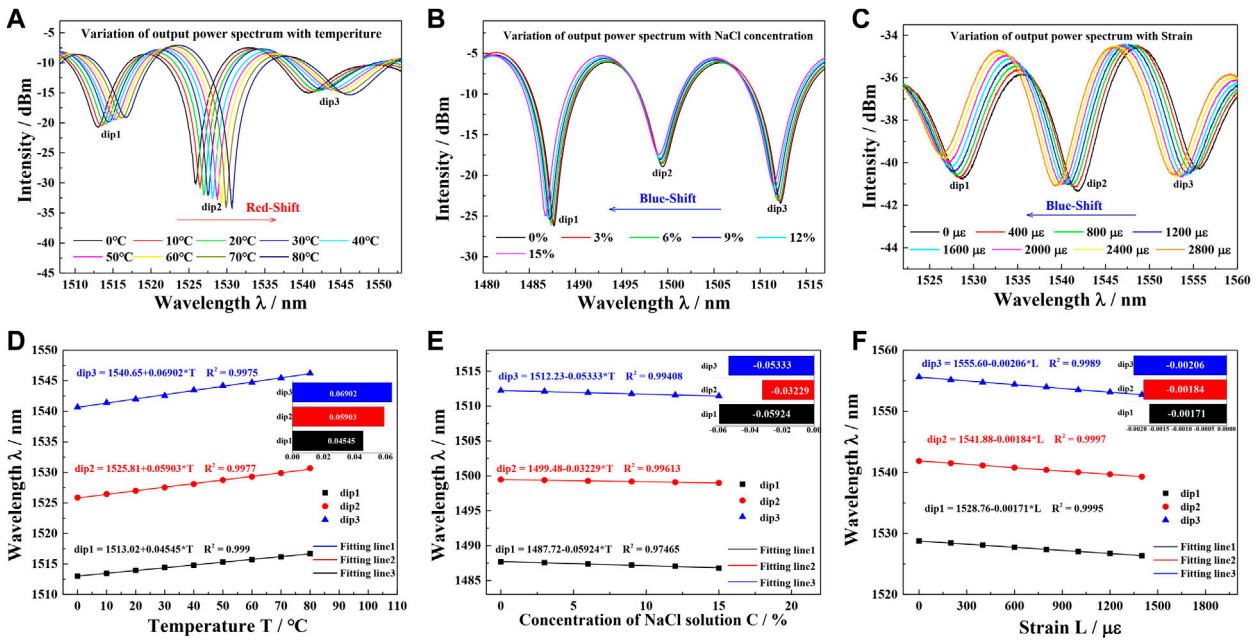

FIGURE 7
The tri-parameter monitoring results, **(A)**, **(B)**, **(C)** experimental transmission spectra under different RI/temperature/strain of surrounding areas; **(D)**, **(E)**, **(F)** the fitted line of dips wavelength shifts with different RI/temperature/strain.

mixing, and is shown in Figure 5C. The degree of drift for each resonance dip is different, demonstrating that the higher order modes could affect drift sensitivity. Figure 5D depicts the changing tendency of the excitation coefficients. With the increasing working wavelength, the effective refractive indexes of the guide modes would decrease slightly. As a result, the excitation coefficients of LP_{01} and LP_{11}^{even} would decline, and those of other modes would rise gradually. Figure 5E presents the shift directions as the variation of the excitation coefficients. One can find that the marked dips show different shift directions and different drift sensitivities. To sum up, the waveform drift is ultimately determined by the Δn_{eff}^{n} and excitation coefficients of guide modes.

3 Experimental methods and discussion

As mentioned above, a precision refractometer with temperature and strain compensated simultaneously could be accomplished with

the structure of ESE. For this purpose, this sensor has been tested under different environments with one variable controlled.

Figure 6A presents the experimental architecture for temperature measurement. The sensor is secured with two fiber clips to prevent transverse bending. The micro-adjusters are applied to obviate the disturbance of the axial micro-strain. All the devices are placed in a temperature control box (WEISS, WT1-180). A broadband source (KOHERAS, superK uersa) serves as a light source. The S + C band range is provided for the sensing system, which is used for conventional communication. As a result, this refractometer could have potential application in remote sensing system. The optical spectrum analyzer (OSA) is used for detecting the interference spectrum. The experimental transmission spectra showing a wavelength red shift corresponding to the temperature of 0°C–80°C, are presented in Figure 7A. The temperature range is divided into nine values (0, 10, 20, 30, 40, 50, 60, 70, 80°C). With the increase of the ambient temperature, the resonant wavelength increases by 4.625 nm on average. A linear relationship between the temperature and resonance wavelength is shown in Figure 7D. The line slopes represent the different drift-sensitivities, which are about ~69.02 pm/°C, ~59.03 pm/°C, and ~45.45 pm/°C, respectively. The average correlation coefficient of polynomial fitting, R^2, is above 0.998, demonstrating very accurate linearity.

Figure 6B shows the SRI experiment, in which this sensor is submerged in NaCl solutions of 0%–15% at 20.0°C with zero strain. The SRI increases in line from 1.3330 to 1.3609 with the concentration of NaCl increasing, which is measured by an Abbe refractometer. The measuring approach is referenced to [28]. In contrast with temperature sensing, the dip wavelength shows a blue shift as depicted in Figure 7B. The accurate linear relationship between SRI and the resonance dips with an average R^2 over 0.988 is shown in Figure 7E. The sensitivities of SRI for each dip are ~28.66 nm/RIU, ~17.35 nm/RIU, and ~31.83 nm/RIU, respectively.

Figure 6C illustrates the experiment of measuring axial micro-strain at room temperature. In it, the sensor could be elongated by the micro-adjuster. The axial strain experiment, Figure 7C, is carried out by elongating the ESE structure at a step of 10 μm, corresponding to 208 με. Similarly, it shows a blue shift. The linear relationship between the axial micro-strain and the resonance dips with an average R^2 over 0.999 is recorded in Figure 7F. The sensitivities for each dip are about ~2.06 pm/με, ~1.84 pm/με, and ~1.71 pm/με, respectively. The fiber-optic SRI sensor exhibits a cross-sensitivity of strain, which is consistent with previous studies [16, 22]. Therefore, an ideal refractometer should be capable of discriminating the strain induced wavelength shift.

To sum up, the linearity of this refractometer is very accurate. In both the simulation and experiment, the resonance dips have their individual sensitivities. In addition, in the experiments, the dips' drift direction is depended on the C_R^n, C_T^n, and C_S^n. As only C_T^n is positive, the interference spectrum would have a red shift as the temperature increasing, while the one would have a blue shift as the SRI or axial micro-strain increasing. However, these coefficients which would affect the experiment result are not considered in the simulation. Thus, the drift direction in the simulation is different from that of experiment. In order to give the experiment direction, the proper simplified condition would be desirable. In short, the calculated results are in good agreement with the experimental data.

The standard matrix inversion method could be used for simultaneous determination of axial micro-strain, temperature, and SRI, when taking C_R^n, C_T^n, and C_S^n as the nth dips' drift slopes. By combining Eqs. 7–9, a matrix equation could be obtained to facilitate discrimination among the three parameters as follows.

$$\begin{bmatrix} \Delta\boldsymbol{\lambda}_{n-1} \\ \Delta\boldsymbol{\lambda}_{n} \\ \Delta\boldsymbol{\lambda}_{n+1} \end{bmatrix} = \begin{bmatrix} \boldsymbol{C}_R^{n-1} & \boldsymbol{C}_T^{n-1} & \boldsymbol{C}_S^{n-1} \\ \boldsymbol{C}_R^{n} & \boldsymbol{C}_T^{n} & \boldsymbol{C}_S^{n} \\ \boldsymbol{C}_R^{n+1} & \boldsymbol{C}_T^{n+1} & \boldsymbol{C}_S^{n+1} \end{bmatrix} \begin{bmatrix} \Delta\boldsymbol{n} \\ \Delta\boldsymbol{T} \\ \Delta\boldsymbol{\varepsilon} \end{bmatrix} = \boldsymbol{M}_{\boldsymbol{R,T,S}} \begin{bmatrix} \Delta\boldsymbol{n} \\ \Delta\boldsymbol{T} \\ \Delta\boldsymbol{\varepsilon} \end{bmatrix} \tag{12}$$

Where $M_{R,T,S}$ is a coefficient matrix. As $M_{R,T,S}$ and $\Delta\lambda_n$ are available through specific experiments, the negative effects of strain and temperature cross sensitivity could be quantified. Thus, by calculating the inverse matrix of the coefficient matrix, $M_{R,T,S}^{-1}$, the error due to temperature and axial micro-strain could be compensated to negligible degree. The proposed approach shows better measurement characteristics than the previous scheme, which usually could only realize temperature or micro-strain compensation. Thus, this SRI sensor is suitable for resolving a high degree of cross-sensitivity.

4 Conclusion

In conclusion, a precision fiber refractometer with temperature and axial micro-strain compensation has been demonstrated. Based on the strict dual-mode EMCF, the in-fiber MZI could obtain a stable clean interference spectrum. This high-quality spectrum is a guarantee for multi-parameter sensing. The FFT analysis of the interference spectrum demonstrates that almost only foundation modes and LP_{11}^{even} are supported. The mechanism of MMI has been developed to interpret the various drift sensitivities and drift direction, which is a novel formulation. By measuring the three dip shifts, the coefficient matrix $M_{R,T,S}$ could be calibrated. Consequently, the three parameters could be measured simultaneously by using the method of spectrum character demodulation. Finally, this refractometer could achieve precision SRI sensing with temperature and axial micro-strain compensation. Therefore, the proposed approach shows great potential for applications in precision SRI measurement with the multi-parameter cross sensitivity [27, 28].

Data availability statement

The raw data supporting the conclusion of this article will be made available by the authors, without undue reservation.

Author contributions

XL: optical experiment, XL and BZ: guidance and revision.

Funding

The authors would like to thank the financial support by the National Natural Science Foundation of China (Grant No. 61905293), the Fundamental Research Funds for the Central University (Grant Nos. 2022QNYL32, 2022QNPY78), the Foundation of Key Laboratory of All Optical Network and Advanced Telecommunication Network, Ministry of Education, China (Beijing Jiaotong University) (Grant No. AON2022001).

Conflict of interest

The authors declare that the research was conducted in the absence of any commercial or financial relationships that could be construed as a potential conflict of interest.

Publisher's note

References

1. Peng Z, Peng Z, Jian J, Wen H, Gribok A, Wang M, et al. Distributed fiber sensor and machine learning data analytics for pipeline protection against extrinsic intrusions and intrinsic corrosions. *Opt Express* (2020) 28:27277–92. doi:10.1364/OE.397509

2. Li J, Zhang J, Sun H, Hong D, Li L, Yang Y, et al. An optical fiber relative humidity sensor based on hollow-core fiber and hydroxypropyl methylcellulose hydrogel film. *Optik* (2019) 195:163172. doi:10.1016/j.ijleo.2019.163172

3. Shang Z, Li S, Li B, Wu H, Sampaolo A, Patimisco P, et al. Quartz-enhanced photoacoustic NH3 sensor exploiting a large-prong-spacing quartz tuning fork and an optical fiber amplifier for biomedical applications. *Photoacoustics* (2022) 26(2022): 100363100363–5979. doi:10.1016/j.pacs.2022.100363,ISSN

4. Alwis LSM, Bremer K, Roth B. Fiber optic sensors embedded in textile-reinforced concrete for smart structural health monitoring: A review. *Sensors* (2021) 21:4948. doi:10.3390/s21154948

5. Chan S, William Y, Wang H-P, Xiang P. Optical fiber sensors for monitoring railway infrastructures: A review towards smart concept. *Symmetry* (2021) 13(12):2251. doi:10.3390/sym13122251

6. Rocha H, Semprimoschnig C, Nunes JP. Sensors for process and structural health monitoring of aerospace composites: A review. *Eng Struct* (2021) 237:112231. doi:10.1016/j.engstruct.2021.112231

7. Goossens S, Berghmans F, Sharif Khodaei Z, Lambinet F, Karachalios E, Saenz-Castillo D, et al. Practicalities of BVID detection on aerospace-grade CFRP materials with optical fibre sensors. *Compos Struct* (2021) 259:113243. doi:10.1016/j.compstruct.2020.113243

8. Yang H, Shin S, Kumar S, Seo D, Oh S, Lee M, et al. A CMOS image sensor based refractometer without spectrometry. *Sensors* (2022) 22(3):1209. doi:10.3390/s22031209

9. Born M, Wolf E. *Principles of optics: Electromagnetic theory of propagation, interference and diffraction of light*. Great Britain: Elsevier (2013).

10. Abbas LG, Ai Z, Mumtaz F, Muhammad A, Dai Y, Parveen R. Temperature and strain sensing with hybrid interferometer. *IEEE Sens J* (2021) 21:26785–92. doi:10.1109/JSEN.2021.3120798

11. Rani S, Haider S, Bukhari SHR, Zaidi SAA, Huda AB. Performance optimization of apodized FBG biomedical sensor for variation in temperature and presence of noise. *IEEJ Trans Electr Electron Eng* (2022) 17:847–55. doi:10.1002/tee.23573

12. Wan H, Zhang J, Chen Q, Wang Z, Zhang Z. An active fiber sensor based on modal interference in few-mode fibers for dual-parameter detection. *Opt Commun* (2021) 481:126498. doi:10.1016/j.optcom.2020.126498

13. Liu Q, Ma Z, Wu Q, Wang W. The biochemical sensor based on liquid-core photonic crystal fiber filled with gold, silver and aluminum. *Opt Laser Technol* (2020) 130:106363. doi:10.1016/j.optlastec.2020.106363

14. Lei X, Dong X, Lu C. Sensitive humidity sensor based on a special dual-mode fiber. *IEEE Sens J* (2019) 19:2587–91. doi:10.1109/JSEN.2018.2889799

15. Ouyang Y, Xu X, Zhao Y, Zhou A, Yuan L. Temperature compensated refractometer based on parallel fiber fabry–pérot interferometers. *IEEE Photon Technol Lett* (2018) 30:1262–5. doi:10.1109/LPT.2018.2844543

16. Kong L-X, Zhang Y-X, Zhang W-G, Li Z, Zhang Y-S, Yan T-Y, et al. Temperature-independent micro-refractometer based on cascaded in-fiber air cavities with strain-error correction. *IEEE Sens J* (2018) 18:8773–80. doi:10.1109/JSEN.2018.2868739

17. Harris J, Lu P, Larocque H, Xu Y, Chen L, Bao X. Highly sensitive in-fiber interferometric refractometer with temperature and axial strain compensation. *Opt Express* (2013) 21:9996. doi:10.1364/OE.21.009996

18. Geisler T, Pedersen ME, Herstrøm S. Measurement of spatial and polarization birefringence in two-mode elliptical core fibers. In: Optical Fiber Communication Conference; 17-21 March 2013; Anaheim, CA, USA. Optica Publishing Group (2013). OW1K. 3.

19. Kim YH, Song KY. Mapping of intermodal beat length distribution in an elliptical-core two-mode fiber based on Brillouin dynamic grating. *Opt Express* (2014) 22:17292. doi:10.1364/OE.22.017292

20. Kasap SO. *Optoelectronics and photonics: Principles and practices*. 2nd ed. Boston: Pearson (2013).

21. Li H, Li H, Meng F, Lou X, Zhu L. All-fiber MZI sensor based on seven-core fiber and fiber ball symmetrical structure. *Opt Lasers Eng* (2019) 112:1–6. doi:10.1016/j.optlaseng.2018.08.021

22. Liang X, Liu S, Li Y, Liu Z, Jian S. Characteristics of a high extinction ratio comb-filter based on LP01–LP11even mode elliptical multilayer-core fibers. *Opt Fiber Technol* (2015) 21:103–9. doi:10.1016/j.yofte.2014.09.005

23. Gloge D. Weakly guiding fibers. *Appl Opt* (1971) 10:2252–8. doi:10.1364/AO.10.002252

24. Li H, Ren G, Atakaramians S, Kuhlmey BT, Jian S. Linearly polarized single TM mode terahertz waveguide. *Opt Lett* (2016) 41:4004. doi:10.1364/OL.41.004004

25. Liang X, Ning T, Li J, Li Y, Liu Z. Axial micro-strain sensor based on resonance demodulation Technology via dual-mode CMECF. *Photonic Sens* (2019) 9:78–88. doi:10.1007/s13320-018-0513-x

26. Zuo B-Z, Liang X, Zhang X-R, Yin T-H. Detection of refractive index with a temperature-compensated MZI-based optical sensor using few-mode fiber. *IEEE Access* (2021) 9:158651–9. doi:10.1109/ACCESS.2021.3130371

27. Chuang SL. *Physics of photonic devices*. Hoboken, New Jersey: John Wiley & Sons (2012).

28. Wu Y, Pei L, Jin W, Jiang Y, Yang Y, Shen Y, et al. Highly sensitive curvature sensor based on asymmetrical twin core fiber and multimode fiber. *Opt Laser Technol* (2017) 92:74–9. doi:10.1016/j.optlastec.2017.01.007